Full Text View

Volume 31, Issue 9 (September 2001)

**Journal of Physical Oceanography**
Article: pp. 2721–2736 | Abstract | PDF (418K)

# Response Characteristics of a Buoyancy-Driven Sea

**T. D. Finnigan, K. B. Winters*, and G. N. Ivey**

*Centre for Water Research, University of Western Australia, Crawley, Western Australia, Australia*

(Manuscript received March 3, 2000, in final form January 23, 2001)

DOI: 10.1175/1520-0485(2001)031<2721:RCOABD>2.0.CO;2

ABSTRACT

The authors consider the flow in a semienclosed sea, or basin, subjected to a destabilizing surface buoyancy flux and separated from a large adjoining reservoir by a sill. A series of numerical experiments were conducted to quantify the energetics of the flow within the basin, that is, the amount of kinetic and potential energy stored within the basin and the rate at which these quantities are transported to and from the reservoir via the exchange flow over the sill. The numerical experiments were formulated at laboratory scales and conducted using a boundary-fitting, clustered grid to resolve the entrainment and mixing processes within the flow and to facilitate quantitative comparison with previous laboratory experiments.

Volume and boundary integrated energetics were computed for both steady and time-varying flows. In the steady-state limit, the rate of energy flux through the surface is balanced by dissipation within the basin and advection of potential energy over the sill and into the reservoir. The analyses focus primarily on this latter quantity because it is closely related to the outflow density and volume transport in two-layered exchange flows. Scaling laws relating the energetics of the flow to the surface buoyancy flux and the geometrical scales of the basin–sill system are derived and validated using the numerical results.

A second set of experiments was conducted to quantify the transient energetics in response to a sudden change in the surface forcing. These results, combined with a linear impulse–response analysis, were used to derive a general expression describing the advection of potential energy across the sill for periodically forced systems. The analytical predictions are shown to compare favorably with directly simulated flows and to be reasonably consistent with limited field observations of the seasonal variability through the Strait of Bab al Mandab.





## 1. Introduction

In many semienclosed seas or basins the large-scale circulation is driven by lateral density gradients. Such buoyancy-driven flows exist, for example, where processes within the sea maintain a net density difference between the sea and adjoining ocean, and therefore produce an exchange of fluid between the two. The dynamics of such systems are of wide

interest because they influence both local and remote oceanic environments (e.g., Reid 1979). This paper investigates the influence on the large-scale flow of mixing processes within a basin (or sea) that is partially separated from a large reservoir (or ocean) by a topographical constriction. We focus in particular on an idealized, convectively driven basin, that is, one subjected to a loss of surface buoyancy due to cooling, evaporation in excess of fresh inflow, or to the growth of sea ice (Fig. 1). The flow configuration is generic, and thus has relevance to semienclosed seas (e.g., the Red Sea), cooling ponds, lake side-arms, and arctic fjords.

There have been several previous studies aimed at modeling similar systems theoretically (e.g., Stommel and Farmer 1953; Phillips 1966; Maxworthy 1997), in the laboratory (Harashima and Watanabe 1986; Sturman and Ivey 1998; Finnigan and Ivey 1999, 2000; Grimm and Maxworthy 1999), and numerically (Kowalik and Matthews 1983). With the exception of Kowalik and Mathews (1983), Sturman and Ivey (1998), and Finnigan and Ivey (1999), these studies have considered only steady flows. Field experiments have also been conducted, most notably in the Red Sea (Murray and Johns 1997; Smeed 1997) and the Mediterranean Sea (Bray et al. 1995; Bryden and Kinder 1991), showing some aspects of the spatial structure and temporal variability of these unsteadily forced systems, particularly in the vicinity of the marginal constriction. In the present work, we consider both steady and unsteady forcing and characterize the spatial and temporal variability of the resulting flow.

We consider flow in the idealized marginal sea configuration shown in Fig. 1. This model system consists of a basin with uniform depth $H$ and width $W$, separated from an ocean of uniform density $\rho_o$ by a sill with minimum depth $h$. An upward flux of buoyancy $B$ through the surface of the basin ($0 \leq x \leq L$, $0 \leq y \leq W$, $z = H$) results in a lateral density gradient across the sill and a consequent buoyancy-driven response.

The surface forcing can be thought of as a flux of available potential energy into the basin. Some of this energy is converted to kinetic energy, associated with both turbulent motions and large-scale circulation and with the exchange flow over the sill. As we will show, an energetics analysis leads to a general description of both the steady and unsteady flow behavior. The potential and kinetic energy stored within the basin, and the flux of these quantities across the sill, can be simply related to the external parameters ($B$, $L$, $W$, $H$, $h$). We focus in particular on the flux of potential energy from the basin, over the sill, and into the adjoining reservoir because this is the energetics quantity most closely related to volumetric and scalar transport. This approach can be applied generally; it does not require that the exchange be reasonably approximated by a layered structure, and thus can be used to quantify the exchange in continuously sheared and stratified flows.

We present results from several numerical experiments based on solutions to the unsteady governing equations in three dimensions. The numerical methods and validation experiments are described in section 2. Numerical simulations allow a volumetric and time-dependent analysis of the energy storage and conversion rates within the basin, as well as the rates of kinetic and potential energy flux across the sill. The results are used to test and validate scaling relationships between energy fluxes and the external parameters characterizing the flow configuration. Steady energetics are described in section 3. The transient response to sudden changes in the surface forcing is discussed in section 4. An impulse–response analysis is used to extend these results to an oscillatory (seasonal or diurnal) forcing in section 5. Concluding remarks appear in section 6.

## 2. Numerical experiments

### *a. Description*

In the laboratory experiments of Finnigan and Ivey (2000) it was found that the internal turbulent stress, or Reynolds stress, contributes significantly to the basin-scale horizontal momentum balance, which, in turn, determines the magnitude of the circulation and therefore the exchange across the sill. Small-scale processes thus influence the large-scale circulation. For the present study we have endeavored to design and implement a series of numerical experiments that represent, as close as possible, the relevant range of flow scales present in these laboratory experiments. To achieve this, the numerical experiments were performed on the same spatial scales as laboratory experiments and high-order methods were employed to solve the unsteady governing equations with fine spatial and temporal resolution (see below). Direct comparisons between laboratory and numerical results provide confidence in the numerical simulations, which are then used to expand the parameter range of the experiments and verify scaling laws based on external parameters. This ultimately leads to a set of general scaling laws that may be used to model the flow response in actual full-scale systems.

Numerical experiments offer a number of conveniences. First, by specifying a semibounded domain we avoid the finite volume restrictions inherent to laboratory experiments. Simulation of slowly varying unsteady flows is thus possible. Furthermore, numerical experiments provide full three-dimensional data fields from which to compute volume and boundary integrated energetics. Finally, the forcing and geometrical parameters can be varied to investigate their effects.

### *b. Methods*

The simulations are based on the equations of motion for incompressible density-stratified flow,

$$\frac{\partial \rho'}{\partial t} + \mathbf{u} \cdot \nabla \rho' = \nabla \cdot K_\rho \nabla \rho', \quad (2)$$

$$\nabla \cdot \mathbf{u} = 0, \quad (3)$$

where $\mathbf{u} = (u, v, w)$ is the velocity vector in Cartesian $(x, y, z)$ coordinates, $\rho'$ is the density perturbation about a constant value $\rho_o$, $p$ is the perturbation about hydrostatic pressure in a fluid with density $\rho(x, y, z, t) = \rho_o + \rho'(x, y, z, t)$, $g$ is the gravitational acceleration, and $\mathbf{z}$ is the unit vector in the vertical direction $z$ (positive upward). The coefficients $K_m$ and $K_\rho$ are the diffusion coefficients for momentum and density, respectively.

Equations (1)–(3) are solved numerically on a three-dimensional orthogonal–curvilinear grid such as that shown in Fig. 2. Details of the methods and solution procedure are given in Winters et al. (2000). The grid spacing is concentrated toward the surface so that relatively strong vertical gradients associated with the forcing surface are accurately resolved. As estimated by Finnigan and Ivey (2000), the smallest turbulence scales expected in the experiments are $\eta \sim 1$ mm. In an effort to resolve the turbulence directly, grids were constructed such that the spacing between computation points was on average $\Delta x \sim \Delta y \sim \Delta z \sim \eta$. A subgrid-scale model, which depends on the local static stability and shear (see Winters and Seim 2000), was employed to enhance diffusion in regions where the turbulence is not adequately resolved. Results indicate that throughout most of the domain the turbulence is well resolved at the grid scale and the subgrid-scale model automatically specifies molecular values for the diffusion coefficients. However, directly under the forcing surface, where the turbulence is most energetic, the model specifies $K_m$ values typically 10%–20% higher than the molecular value $\nu = 10^{-6}$.

The boundary conditions were chosen to match those of the laboratory experiments. Referring to Fig. 2, the lower, upper, and left side boundaries have $\mathbf{u} = 0$. With the exception of the forced region of the surface, we specify $\partial\rho/\partial\hat{\mathbf{n}} = 0$ over these boundaries, where $\mathbf{n}$ is the unit normal vector for each surface. These conditions correspond to those for a no-slip insulated boundary. Over the area defined by $0 \le x/L \le 1$, $0 \le y/W \le 1$, and $z/H = 1$ we impose a buoyancy flux (per unit area),

$$B = \frac{g}{\rho_0} K_\rho \frac{\partial \rho'}{\partial z}, \quad (4)$$

by specifying nonzero $\partial\rho'/\partial z|_{z=H}$. The remainder of the upper surface is insulated. Conditions are periodic between the front ($y/W = 0$) and back ($y/W = 1$) boundaries, and we therefore effectively simulate the flow in a "slice" of width $W$ along the axis of a laboratory tank like that of Finnigan and Ivey (2000). At the open right boundary, an Orlanski-type radiation condition is used for momentum. The inflow density is held fixed at the ambient value $\rho_o$, while $\partial\rho'/\partial x = 0$ is imposed on the outflow. A boundary condition is also required for pressure at the open boundaries. Periodicity is imposed in the $y$ direction while at the right boundary a time-dependent Dirichlet condition corresponding to hydrostatic pressure is employed. We note that the right-hand boundary has been placed at the foot of the sill on the outside of the basin, that is, at a location where the flow is expected to be largely horizontal and stably stratified.

### *c. Experiments*

We conducted a total of 12 numerical experiments as listed in Table 1. Experiments 1–7 demonstrate the effects of varying $B$ and $L$ and experiments 8–11 explore the dependence on the relative sill depth $H/h$. Each of these experiments contains both an unsteady phase and a steady-state phase. Experiment 12 was performed to investigate the response to oscillatory forcing. Referring to Table 1, the initial state of each experiment is indicated by the value of $B_o$ that pertains to time $t < 0$. $B_o = 0$ indicates a flow that is initially at rest and unforced. The experiment begins at time $t = 0$ when the forcing $B = B_\infty$ is suddenly imposed. For experiments with $B_o \neq 0$ the flow for $t < 0$ is already at steady state and forced with the constant value $B = B_o$ indicated in the table. In these cases, the forcing is suddenly changed at $t = 0$ and the flow adjusts in response to the change. The rightmost column in Table 1 refers to the forcing functions shown in Fig. 3. Where the forcing for $t > 0$ is constant the flow eventually reaches a new steady state. In experiment 12 the forcing is time dependent and while the flow does not become steady, it does achieve an oscillatory state with a steady mean as will be described in section 5.

### *d. Comparisons between laboratory and numerical results*

#### 1) TEMPORAL AND SPATIAL FLOW FEATURES

For the type of flows considered here, Finnigan and Ivey (1999) described the unsteady adjustment following application of the forcing. As they showed, the outward flux of buoyancy from the surface of the basin leads to turbulent convective motions that mix relatively dense fluid downward. The mean density of the basin was found to increase with time according to

$$\rho \sim \frac{\rho_o}{g}\frac{Bt}{H}. \qquad (5)$$

This increases the density contrast between the fluid in the basin and the adjoining reservoir.

Driven by this density contrast, the ensuing adjustment is characterized by two sequential stages. During the first stage the basin is continually mixed by convective turbulence with zero mean flow in the interior and an accelerating exchange flow over the sill. In the second stage the exchange flow develops further and slowly extends into the basin. The final steady state has an exchange flow that occupies the entire length of the basin. In Fig. 4 results from numerical experiment 1 are used as an example to demonstrate the unsteady adjustment. Velocity and density data were extracted along a central vertical ($x$–$z$) plane at specific times during each of the three stages just described.

2) UNSTEADY FLOW AT THE SILL

Following the initiation of buoyancy forcing $B$ at time $t = 0$ the velocity at the sill was shown to develop as

first unsteady stage:

$$u \sim \frac{Bt^2}{l}, \qquad t \lesssim t_t \qquad (6)$$

second unsteady stage:

$$u \sim \left(\frac{Bht}{H}\right)^{1/2}, \qquad t_t \lesssim t \lesssim t_{ss} \qquad (7)$$

steady state:

$$u \sim (BL)^{1/3}, \qquad t \gtrsim t_{ss} \qquad (8)$$

where $t_t$ is the time of transition from the first to the second stage and

$$t_{ss} \sim L^{2/3}B^{-1/3}\left(\frac{H}{h}\right) \qquad (9)$$

is the time required for the flow to reach steady state. Since $t_t \ll t_{tt}$ (see Finnigan and Ivey 1999), we focus our attention on the second stage and the steady state. The volume flux per unit width $q \sim uh$ implying from (7),

$$q \sim \left(\frac{Bt}{H}\right)^{1/2} h^{3/2}, \qquad (10)$$

and therefore,

$$\frac{q}{(B/H)^{1/2}h^{3/2}} \sim t^{1/2}. \qquad (11)$$

Numerical experiment 1 and laboratory experiment L (see Table 1) were configured similarly and are therefore suitable for comparison. In Fig. 5 we present results for the time-varying volume flow rate, determined in both cases by

$$q(t) = \int_i^H u_s(z, t)\, dz, \qquad (12)$$

where $u_s(z, t)$ represents vertical profiles (from a single location in $y$) of the horizontal velocity component at the sill crest and $z = i$ indicates the level at which $u_s = 0$, or the velocity interface. The results for $q$ were scaled according to (11) and the time axis was scaled as $t/t_{ss}$. While the two experiments had slightly different external parameters the results are similar in both magnitude and temporal variation. This indicates that the scaling results (9) and (10) are appropriate and the numerical simulations are in quantitative agreement with the laboratory results. We hypothesize that the irregular peaks in the laboratory data are due to basin-scale internal waves or pressure pulses from a particle injector that was situated slightly

upstream of the basin inflow.

3) STEADY-STATE HORIZONTAL TRANSECTS

*(i) Velocity scaling*

In the basin interior the steady-state mean horizontal velocity component of the upper layer is expected to vary as $u \sim (Bx)^{1/3}$ (Phillips 1966; Finnigan and Ivey 2000) and therefore $|u^3/B| \sim x$. Horizontal transects of this quantity were obtained from results of two typical numerical experiments (1 and 6) with different values of $L$ and from the laboratory experiment L. These are shown in Fig. 6. A variation, consistent with the scaling, is observed in a central region of the basin away from endwall and sill effects. The width of the sill relative to the length of the basin is significantly greater for experiment 1 than for experiments 6 and L, and the effect of this is evident in the range $x/L > 0.7$. Nevertheless, all three sets of results concur in the central region.

*(ii) Density scaling and the role of the basin aspect ratio L/h*

The alongchannel variation of density can be characterized by the reduced gravity,

$$g'(x) = g\frac{\rho_2 - \rho_1}{\rho_2}, \qquad (13)$$

where $\rho_1$ and $\rho_2$ are characteristic density values in the upper (inflowing) and lower (outflowing) layers, respectively. From the numerical results, horizontal transects of $\rho_1$ and $\rho_2$ are obtained by averaging vertically across the layers delineated by the velocity interface $u = 0$. This allows a comparison with previous laboratory results, which were interpreted using (13).

In Grimm and Maxworthy's (1999) experiments $g'$ was found to scale as $B^{2/3}x/h^{4/3}$ when the aspect ratio $L/h > 20$. In their experiments vertical mixing was confined to a relatively small region near the closed end of the basin. The $g'$ scaling was observed to change when $L/h < 20$ since the mixing region then occupied a significant portion of the basin. Their observations are in general agreement with the arguments of Finnigan and Ivey (2000), who showed that such mixing can only occur within a distance of about $10h$ from the endwall. For $x \gtrsim 10h$ the density difference between layers is large enough to suppress mixing.

Figure 7a shows the horizontal variation of $g'$, obtained from the steady-state results of two typical experiments (1 and 6), and scaled such that $g' \sim B^{2/3}x/h^{4/3}$, as suggested by Maxworthy (1997). The solid line represents a least squares fit to the laboratory results of Grimm and Maxworthy (1999). The aspect ratio $L/h > 20$ for both the laboratory experiments and experiment 6 and the results scale similarly. For experiment 1 $L/h = 10$ and the results scale differently, due to the effects of mixing.

We now refer to Fig. 7b, which shows the same numerical results rescaled such that $g' \sim (Bx)^{2/3}/h$ (Phillips 1966), a form more appropriate for mixing-dominated flows. This scaling brings the two sets of results closer together, therefore indicating that experiment 6 ($L/h = 30$) also scales somewhat like the shorter, mixing-dominated basin. Experiment 6 must therefore lie in a transition region between the two scaling laws and, in summary, we suggest that

$$g'(x) \sim \frac{(Bx)^{2/3}}{h} \quad \text{for } \frac{L}{h} \lesssim 30 \qquad (14)$$

$$g'(x) \sim \frac{B^{2/3}x}{x^{4/3}} \quad \text{for } \frac{L}{h} \gtrsim 30, \qquad (15)$$

where the transition at $L/h \approx 30$ is gradual. More extensive experimental work is required to determine the precise threshold between the scaling regimes. Since all of our numerical experiments have $L/h \lesssim 30$, we shall generally use (14) in applications to our numerical results. In applications to longer basins we will employ (15).

## 3. Steady energetics

### *a. Energy storage and flux*

The experimental flows are driven by a diffusive flux of available potential energy into the basin through the upper surface. The resulting static instability leads to conversion of this potential energy to kinetic energy. The potential energy stored in the basin control volume ($V$), shown in Fig. 8, is given by

and the stored kinetic energy by

$$E_k = \int_V \rho_o \frac{1}{2}(u^2 + v^2 + w^2)\, dV. \qquad (17)$$

Here $E_p$ is expressed relative to the energy stored in a basin of uniform density $\rho_o$. The rate of change of $E_p$ and $E_k$ are written as

$$\frac{dE_p}{dt} = \underbrace{-g \oint_{S_s} \rho_s' z u_s \, dS_s}_{\text{as}_p} + \underbrace{g \int_V \rho' w \, dV}_{\text{bf}} + \underbrace{g \oint_{S_H} K_\rho z \frac{\partial \rho_H'}{\partial z} \, dS_H}_{\text{sd}} - \underbrace{g \int_V \nabla K_\rho z \cdot \nabla \rho' \, dV}_{\text{id}}, \qquad (18)$$

$$\frac{dE_k}{dt} = \underbrace{-\oint_{S_s} u_s p_s \, dS_s}_{\text{pw}} + \underbrace{\rho_o \oint_{S_s} u_s \frac{1}{2}(u_s^2 + v_s^2 + w_s^2) \, dS_s}_{\text{as}_k} - \underbrace{g \int_V \rho' w \, dV}_{\text{bf}} + \underbrace{\rho_o \int_V \mathbf{u} \cdot \nabla (K_m \nabla \cdot \mathbf{u}) \, dV}_{\text{e}}, \qquad (19)$$

*(Click the equation graphic to enlarge/reduce size)*

where the subscript *s* indicates quantities at the sill crest and subscript *H* indicates quantities at the surface, and therefore $S_s$ and $S_H$ represent the vertical and horizontal surface areas of the control volume at these locations, respectively (see Fig. 8). On the right side of (18) the individual terms are described as follows: advection of potential energy across the vertical boundary at the sill ($\text{as}_p$), buoyancy flux (bf), diffusive flux of potential energy through the surface (sd), and the change in potential energy due to internal vertical diffusion (id). Similarly, in (19) the terms may be described as pressure work at the sill boundary (pw), advection of kinetic energy across the sill ($\text{as}_k$), buoyancy flux (bf), and the rate of dissipation of kinetic energy (e). Note that the transfer of energy between the potential and kinetic energy fields is through the buoyancy flux, which appears with opposite sign in both (18) and (19).

The three-dimensional time-dependent simulation results are used to calculate time series for each of the terms shown in (18) and (19). As an example, Fig. 9 shows the time series results from experiment 1, which demonstrates how each of these quantities varies as the flow adjusts from the initial rest state to the final steady state. After the initial unsteady period ($0 \leq t \leq 625$ s), which was described above in section 2d(2), we note that $dE_p/dt = dE_k/dt \rightarrow 0$ and the flux quantities approach constant values. The shaded region in Fig. 9 indicates the steady state, during which we observe that the dominant terms in (18) are sd, $\text{as}_p$, and bf and in (19) they are bf and e.

### *b. Scaling*

#### 1) ENERGY STORAGE: $E_P$ AND $E_K$

Following the arguments of Phillips (1966) and Finnigan and Ivey (2000) the characteristic density scale for the basin as a whole is

$$\rho' \sim \frac{\rho_o}{g} \frac{(BL)^{2/3}}{H}, \qquad (20)$$

where *H* is taken as the more relevant vertical length scale in this context. Here we have used the density scaling in (14) for basins with $L/h \lesssim 30$. The results differ only slightly if (15) is used instead.

When the sill is short relative to the total length of the basin the volume $V \sim LHW$ and from (16) and (20) we find

$$E_p \sim \rho_o B^{2/3} L^{5/3} HW. \qquad (21)$$

We also expect $E_p$ to depend on the sill depth *h*. In this configuration the two vertical lengthscales, *H* and *h*, both influence the flow but without further idealization and/or theoretical development, it will be difficult to incorporate the influence of this parameter. Invoking an idealized model of the flow at the sill (such as internal hydraulic theory) is inappropriate since it would introduce additional variables. Furthermore, such theories apply only under certain conditions. In order to maintain generality we choose to incorporate the effect of the sill with a dimensionless term $(H/h)^\gamma$ such that

$$E_p \sim \rho_o B^{2/3} L^{5/3} HW(H/h)^{\gamma}, \quad (22)$$

where $\gamma$ is an unknown constant. We have thus incorporated the relative effect of the two vertical lengthscales ($H$ and $h$), the weighting to be given by the experimental determination of the constant $\gamma$. This allows a simple description of the behavior without assumptions regarding the detailed structure of the flow over the sill.

The kinetic energy stored in the basin is related to the mean velocity field, which is dominated by a horizontal exchange flow with velocity $u \sim (BL)^{1/3}$ (Phillips 1966; Finnigan and Ivey 2000). From (17) we therefore write

$$E_k \sim \rho_o B^{2/3} L^{5/3} HW(H/h)^{\delta}, \quad (23)$$

where the $(H/h)^{\delta}$ term arises by the same dimensional reasoning as for $E_p$. Clearly, for larger values of $H/h$ the exchange between the basin and reservoir is restricted. We allow for different exponents for $H/h$ in (22) and (23) because we expect, for example, that the stored potential energy must increase with $H/h$ while the stored kinetic energy must decrease with $H/h$.

We can investigate this dependence by considering the three experiments (9, 10, and 11) between which only $h$ was varied. Time-averaged results from the steady-state portion of these experiments are shown in Fig. 10. The linear trend for both $E_p$ and $E_k$ supports the scaling with respect to $h$ and the slopes of lines fitted by the least squares method provide estimates for the values of $\gamma$ and $\delta$ (see Table 2). As expected $\gamma > 0$ and $\delta < 0$. With these values known we can now test the scaling laws (22) and (23) against the whole range of experiments. Results are shown in Fig. 11 where a linear fit to the $E_p$ data shows that (22) is valid over the parameter range considered. More scatter is observed in the results for $E_k$, but a linear trend is still evident. Proportionality constants ($c_p$ and $c_k$), obtained from the slope of the data in Fig. 11a and 11b, respectively, may be used to relate the simulation results directly to the scaled forms (22) and (23). The resulting formulas are listed in Table 2 and will be used in subsequent sections.

2) ENERGY FLUXES

There is a constant flux of energy through the control volume, supplied via a diffusive flux of potential energy at the surface. The results in Fig. 9 showed that the dominant terms in the steady budget are sd, $as_p$, bf, and e. By eliminating the buoyancy flux bf between (18) and (19) and neglecting relatively small terms the steady budget can be approximated as

$$as_p = sd + e, \quad (24)$$

where the dissipation term $e$ is always negative. The imposed flux sd can be written

$$sd = g \oint_{S_H} K_\rho z \frac{\partial \rho'_H}{\partial z} \, dS_H = \rho_o BLHW. \quad (25)$$

Measurements of steady buoyancy-driven convection (e.g., Anis and Moum 1994) have shown that the dissipation rate $\epsilon \sim B$, which corresponds to assuming $e \sim sd$ in our notation. However, the basin is subject to a lateral exchange and, as argued above, the sill depth must influence the energetics. We therefore bring in the relative influence of vertical lengthscales by writing

$$e \sim (sd)(H/h)^{\zeta}, \quad (26)$$

where $\zeta$ is an undetermined constant.

At the sill the scale of vertical density variations is $\rho'_s \sim (\rho_o/g)(BL)^{2/3}/h$ (Phillips 1966; Finnigan and Ivey 2000). Note that $\rho'_s > \rho'$, which characterizes the basin as a whole. The advection of potential energy across the sill may now be written as

$$as_p = -g \oint_{S_s} \rho'_s z u_s \, dS_s \sim \rho_o BLHW, \quad (27)$$

where $u_s \sim (BL)^{1/3}$, $S_s \sim hW$, and $z \sim H$ is the characteristic height of the flow at the sill. Although this suggests that $as_p$ scales in direct proportion to sd, we again introduce an additional dependence on the relative sill depth $H/h$ and write

$$as_p \sim (sd)(H/h)^{\lambda}, \quad (28)$$

where $\lambda$ is an unknown constant.

Time-averaged steady-state values of each of the flux quantities defined above in (18) and (19) are shown in Table 3 for each experiment, except experiment 12 which is unsteady. In each case averages were computed over steady-state time segments, such as that shown for experiment 1 as a shaded region in Fig. 9. Table 3 shows that the dominant energy flux balance (24), identified in section 3a for experiment 1, holds generally for all of the experiments. The normalized fluxes are roughly constant for experiments 1–7, between which only $B$ and $L$ were varied, and it therefore follows that these quantities scale with sd. However, the normalized fluxes, particularly $as_{pn}$ and $e_n$, are significantly different in experiments 9, 10, and 11, between which only $H/h$ was varied. Therefore, the relative sill depth $H/h$ has a significant influence on the scaling and we find that the simulation results are reasonably well described by the simple forms of (26) and (28).

The potential energy $E_{pn}$ consistently represents about 98% of the total stored energy when $H/h = 2$. When $H/h = 1.3$, $E_{pn}$ drops to about 90% and $E_{kn}$ increases commensurately. This occurs because a deeper sill not only allows a higher exchange rate, it also decreases the density of the outflow since the inflowing fluid moves more quickly past the forcing surface and allows it to exit the basin at a lower height. The values obtained for $\gamma$ and $\delta$ are therefore consistent with the observations in general.

The value of $\lambda$ in (28) is estimated using steady-state results from experiments 9, 10, and 11 as shown in Fig. 12. With this result (see Table 2) we now apply the scaling (28) to all of the experiments. As shown in Fig. 13, there is a clear correlation between computed $as_p$ values and $\rho_o BLHW(H/L)^{\lambda}$. Table 2 summarizes the scaling relationships and experimentally determined constants for the important energetics quantities and the response timescale (described below in section 4).

The storage and flux of energy in the basin control volume is shown graphically in Fig. 14. The bracketed terms are derived from Table 2 by averaging over the values from experiments 1–7, for which $H/h = 2$. These results demonstrate that for every unit of potential energy input through the surface, 0.53 units are transferred to kinetic energy via buoyancy flux. Of this, 0.36 units get dissipated (or converted to internal energy) within the basin. Most of the remaining kinetic energy goes into pressure work at the sill boundary while a small amount is advected out of the basin. Almost all of the potential energy that is not transferred to the kinetic energy field is advected out of the basin across the sill. Vertical diffusion within the basin acts as a small source of potential energy (see also Fig. 9).

### *c. The physical relevance of $as_p$*

In the previous studies by Finnigan and Ivey (1999, 2000) and Grimm and Maxworthy (1999) the exchange flow in the vicinity of the sill was assumed to consist of two distinct layers within which the density was constant and the velocity purely horizontal. Such idealizations provide useful interpretations using the theory of internal hydraulics. In translating the results of such studies back to actual geophysical flows one is however faced with the realization that the assumptions underlying hydraulic theory are often violated in nature (Bray et al. 1995; Gregg et al. 1999).

Consideration of the flux of potential energy across the sill requires no assumptions regarding the physical structure of the flow. Therefore $as_p$ offers a more general description of the exchange than either the volume flux $q_s$ or the reduced gravity $g'$, both of which are difficult to isolate unless the flow is assumed to be "two-layered."

Nevertheless, if the exchange can be considered two-layered, then for relatively short basins ($H/h < 30$) we have $q_s \sim (BL)^{1/3}h$ and $g' \sim (BL)^{2/3}/h$, while for long basins ($H/h > 30$) $q_s \sim B^{1/3}h^{4/3}$ and $g' \sim B^{2/3}L/h^{4/3}$ [see section 2d(3)]. In both cases the scaling satisfies the buoyancy conservation condition $g'q_s = BL$ and we can therefore write (28) as

$$as_p \sim \rho_o g' q_s HW(H/h)^{\lambda}, \quad (29)$$

which yields a relationship between $as_p$, $g'$, and $q_s$. For practical purposes, if $as_p$ can be estimated from (28) and $g'$ measured at the sill, then (29) may be used to determine $q_s$.

In the more realistic situation when the flow is not two-layered, but rather characterized by continuous density profiles $\rho(z)$, then conservation of buoyancy implies that

$$BL = \frac{g}{\rho_o}\int_{H-h}^{H} \rho'(z)u_s(z)\,dz, \quad (30)$$

and (29) becomes (up to a constant)

$$\left( \frac{}{J_{H-h}} \right)$$

in which case $q_s$ is not easily isolated. Depending on the complexity of the $\rho'_s$ and $u_s$ profiles these may be nontrivial to separate. If the stratification is near linear, then one might estimate $\rho'_s \sim (\rho_o/g)N^2h$, where $N$ is the buoyancy frequency, and therefore as$_p \sim \rho_o N^2 h q_s HW(H/h)^{\lambda}$; however, this is but a rough approximation.

**4. Unsteady response**

We have presented results for steady-state flows and shown how certain energetics quantities ($E_p$, $E_k$, and as$_p$) scale with the external parameters. We now build on these findings by investigating how these quantities respond in time after an abrupt change in forcing is imposed. Results from this section will then be used in our treatment of the response to periodic forcing functions (section 5).

*a. Time scaling*

We consider the situation where the initial state of the flow is one of steady motion in balance with a constant surface buoyancy flux $B = B_o$. At time $t = 0$ the forcing is suddenly increased (or decreased) to a value $B_\infty$ and thereafter held constant. For $t > 0$ the flow adjusts to the step change in forcing and it gradually approaches a new steady state. This is an idealized representation of the response of a semienclosed sea to a change in the surface buoyancy flux that occurs rapidly relative to the time required for the flow to adjust.

A scale that characterizes the time required for the flow to adjust from rest to steady state was described in section 2d(2). The response timescale is determined as the difference between the steady-state timescales ($t_{ss}$) for the initial forcing value ($B_o$) and that imposed after the step ($B_\infty$). It is therefore expressed as

$$t_r \sim L^{2/3}(B_\infty - B_o)^{-1/3}(H/h)^{\tilde{\xi}}, \quad (32)$$

where we have included the exponent ($\tilde{\xi}$) by the same reasoning as above for the energetics.

*b. Rate of change of $E_p$ and $E_k$*

A sudden change in the flux of potential energy through the surface results in a gradual change in the volume-integrated energies $E_p$ and $E_k$. During the adjustment period $dE_p/dt$ and $dE_k/dt$ are nonzero. We begin by quantifying the rate at which a steady state is reestablished, focusing on sudden increases in $B$, that is, experiments 2, 3, and 7.

Figure 15a shows the changes in potential energy following a step increase in $B$. The quantity $E_{p_*}$ is the deviation of $E_p(t)$ from the initial steady state $E_{po}$, normalized by the steady-state scaling such that

$$E_{p*} = \frac{E_p(t) - E_{po}}{c_p \rho_o L^{5/3}(B_\infty^{2/3} - B_o^{2/3})HW(H/h)^{\gamma}}, \quad (33)$$

(see Table 2). Time is scaled by the time required for the flow to reach steady state, and we therefore define the dimensionless timescale $t_* = t/t_r$. With these definitions both $E_{p_*}$ and $t_*$ have values of unity at the moment the flow reaches steady state. The coalescence of data from the three experiments indicates that both the energy scaling and the response-time scaling are appropriate. The experimentally determined constants associated with the timescale $t_r$ are shown in Table 2.

The kinetic energy is shown in Fig. 15b where $E_k$ is normalized via

$$E_{k*} = \frac{E_k(t) - E_{ko}}{c_k \rho_o L^{5/3}(B_\infty^{2/3} - B_o^{2/3})HW(H/h)^{\delta}}. \quad (34)$$

The scaled results for the three experiments respond similarly and generally follow the same curve as for $E_{p_*}$. Oscillations of unknown origin are more evident in $E_{k_*}$ than in $E_{p_*}$.

We assume that the rate of change of $E_p$ and $E_k$ depends on how close the system is to steady state. We therefore

suggest that the normalized stored potential and kinetic energy vary as

$$E_{p_*}(t_*) = E_{k_*}(t_*) = 1 - e^{-\alpha_* t_*}, \quad (35)$$

where $\alpha_*$ is the dimensionless attenuation coefficient. Fitting (35) to the data shown in both Fig. 15a and 15b gives $\alpha_* = 4 \pm 0.2$, where the error is associated with the difference between best-fit lines in each figure. Note the system time constant $tc = t_r \alpha_*^{-1}$. The time derivatives are determined from (35) as

$$\frac{dE_{p*}}{dt_*} = \frac{dE_{k*}}{dt_*} = \alpha_* e^{-\alpha_* t_*}, \quad (36)$$

which will now be used in the interpretation of the unsteady response of flow over the sill.

### *c. Unsteady response of as$_p$*

In section 3b(2) we used (18) and (19) to derive a steady-state equation (28) for as$_p$ (also see Table 2). We now seek an equation for the unsteady response to a step function input with magnitude $\Delta B = B_\infty - B_o$. The dominant terms in (18) and (19) combine to give

$$\mathrm{as}_p(t) = \left[ -\frac{dE_p}{dt} - \frac{dE_k}{dt} + \mathrm{sd} + e \right] \mathcal{H}(t) + \mathrm{as}_{po}, \quad (37)$$

where $\mathcal{H}(t)$ is the Heaviside stepfunction defined such that

$$\mathcal{H}(t) = \begin{cases} 0 & \text{for } t < 0 \\ 1 & \text{for } t > 0, \end{cases} \quad (38)$$

and as$_{po}$ is the initial condition ($t < 0$). We now define the normalized advection of potential energy across the sill as

$$\mathrm{as}_{p*}(t_*) = \frac{\mathrm{as}_p(t) - \mathrm{as}_{po}}{\rho_o \Delta B L H W \left(\frac{H}{h}\right)^{\lambda}}, \quad (39)$$

and with (36), and the definitions (33) and (34),

$$\mathrm{as}_{p*}(t_*) = \left\{ \frac{-\alpha_*}{c_s c_t (H/h)^{\lambda+\xi}} \times \left[ c_p \left(\frac{H}{h}\right)^{\gamma} + c_k \left(\frac{H}{h}\right)^{\delta} \right] e^{-\alpha_* t_*} + 1 \right\} \mathcal{H}(t_*), \quad (40)$$

where we have substituted $\alpha_* t_* = \alpha t$ and utilized the fact that $(B^{2/3}_\infty - B^{2/3}_o)(B_\infty - B_o) \approx \Delta B$. The terms within braces represent the transient response and the forcing term. The form of (40) is typical of classical mechanical systems that exhibit a first-order time-invariant response to a step function input. Here we have assumed a "slowly varying" flow for which the steady scaling arguments of section 3b(1) are approximately valid at any instant.

The initial conditions require that as$_{p_*} = 0$ at $t_* = 0$ and it follows from (40) that the transient term has a value of $-1$ at $t_* = 0$ and therefore

$$\xi = \frac{\left[c_s c_i\left[\quad (h) \quad (h)\right]\right]}{\ln\left(\frac{H}{h}\right)} - \lambda, \qquad (41)$$

which suggests that $\xi$, the exponent in the timescale (32), is itself a function of the ratio $H/h$. Mathematically, this is a consequence of introducing $H/h$ in the scaling for $E_p$ and $E_k$. It turns out that $\xi$ is a weak function of $H/h$ with values $O(1)$ for moderate sill depths (i.e., $H/h = 2$).

The unsteady response of the advection of potential energy across the sill may now be written simply as

$$\mathrm{as}_{p_*}(t_*) = [1 - e^{-\alpha_* t_*}]\mathcal{H}(t_*), \quad (42)$$

which is shown in Fig. 16 along with results from experiments 2, 3, and 7. The agreement between the experimental and analytical results provides confidence in the assumptions and scaling laws developed above. The response equation (42) is generally applicable and, with the information provided in Table 2 and the definition (39), one can see that it is simply a function of $L$, $H$, $h$, $W$, $B_o$, and $B_\infty$.

## 5. Periodic forcing

The steady forcing and step function unsteady forcing scenarios considered in the previous sections may mimic situations found in nature under specific isolated conditions. More generally, semienclosed seas and other similar water bodies experience a surface buoyancy flux that is continuously varying and often periodic. Smaller systems are forced by diurnal heating and cooling. Larger systems, such as the Red Sea, are forced by the seasonal variation of the evaporation rate. We now consider this type of forcing and the associated flow response.

### *a. The transfer function*

The response equation for a step function input was developed in section 4c where it was noted that the system resembles one that exhibits a first-order linear response. Using the results obtained above, we now seek a more general formulation for the response to an arbitrary forcing function.

We focus here on forcing scenarios that are periodic in time. For such functions, the complex frequency is defined as $s = i\omega$ where $i = (-1)^{1/2}$, or in dimensionless form $s_* = i\omega_*$ where $\omega_* = \omega t_r$. Under step function forcing, the response equation (42) may be translated into complex frequency space by taking the Laplace transform such that

$$\mathcal{L}[\mathrm{as}_{p*}] = \mathbf{as}_{p*}(s_*) = \frac{1}{s_*} - \frac{1}{s_* + \alpha_*}, \qquad (43)$$

or by isolating the transform of the step function $1/s_*$,

$$\mathbf{as}_{p*}(s_*) = \underbrace{\left[1 - \frac{s_*}{s_* + \alpha_*}\right]}_{\mathbf{T}(s_*)} \underbrace{\frac{1}{s_*}}_{\mathbf{F}(s_*)}, \qquad (44)$$

where $\mathbf{T}(s_*)$ is the transfer function and $\mathbf{F}(s_*)$ is the transformed step-forcing function (e.g., Sanford 1965). The transfer function is independent of the forcing function yet it contains the natural attenuation and frequency response characteristics of the system. Note that $\mathbf{T}(s_*)$ is a function of $s_*$ and $\alpha_*$, which, when dimensionalized, depend on the driving frequency $\omega$ and the attenuation coefficient $\alpha$, respectively, along with the external parameters ($L$, $H$, $h$, $W$, $B_o$, $B_\infty$). When multiplied by any transformed forcing function, $\mathbf{T}(s_*)$ effectively transfers the signal through the system to the output, which in this case is the advection of potential energy over the sill $\mathbf{as}_{p_*}(s_*)$.

### *b. Sinusoidal forcing*

We now consider a situation in which the flow is initially at steady state in balance with a surface buoyancy flux $B = B_o$ (for $t < 0$). At time $t = 0$ the surface buoyancy flux $B(t)$ suddenly begins to oscillate sinusoidally about $B_o$. The unsteady

forcing term is therefore

$$F_s(t) = [B_s \sin(\omega t)]\mathcal{H}(t), \quad (45)$$

where $B_s$ is the amplitude of the oscillation. In the frequency domain the nondimensional response to this input function is simply

$$\mathbf{as}_{p*}(s_*) = \mathbf{T}(s_*)\mathbf{F}_s(s_*) \quad \text{and} \quad (46)$$

$$\mathbf{as}_{p*}(s_*) = \left[\frac{\alpha_*}{s_* + \alpha_*}\right]\left(\frac{\omega_* B_*}{s_*^2 + \omega_*^2}\right), \quad (47)$$

where $B_* = B_s/\Delta B$. The inverse Laplace transform of (47) gives the response equation for $as_{p_*}(t_*)$ in the time domain. By a partial fraction expansion this is found to be

$$as_{p*}(t_*) = [K_1 e^{-\alpha_* t_*} + K_2 \sin(\omega_* t_* + \phi)]\mathcal{H}(t_*), \quad (48)$$

where

$$K_1 = \frac{\alpha_* \omega_* B_*}{\alpha_*^2 + \omega_*^2}, \quad (49)$$

$$K_2 = \frac{B_* \alpha_*}{(\alpha_*^2 + \omega_*^2)^{1/2}}, \quad \text{and} \quad (50)$$

$$\phi = \tan^{-1}\left(-\frac{\omega_*}{\alpha_*}\right), \quad (51)$$

which is again simply a function of the external parameters, the attenuation coefficient, and the parameters that characterize the input function ($B_s$, $\omega$). The first term in (48) represents the small time unsteady adjustment following a step increase at $t = 0$ and the second term represents the unsteady response to continued periodic forcing. Only the second term is important for $t \gg 0$ and in the absence of a step increase in $B_o$.

The steady scaling of section 3b(2) shows that $as_p = c_s \mathrm{sd}(H/h)^{\lambda}$, while the long term ($t \gg 0$) unsteady response (48) implies that the amplitude ($K_2$) under sinusoidal forcing is modulated by a factor $\alpha/(\alpha^2 + \omega^2)^{1/2}$. This effect is shown in Fig. 17, which demonstrates how the magnitude ($K_2$) and phase ($\Phi$) of the response depend on frequency. For low frequencies ($\omega \ll 1/t_r$) the magnitude approaches that indicated by the steady-state scaling of section 3b(2) and the response is "in-phase" with the forcing. As the frequency is increased the magnitude decreases and the response lags the forcing. At high frequencies ($\omega \gg 1/t_r$) the oscillation of the forcing at the surface is completely damped within the system and the flow over the sill is essentially steady, that is, $K_2 = 0$. In Fig. 17a, the absence of a local maximum at a nonzero frequency signifies that there is no *resonant* frequency as expected in a dissipative system.

### *c. Applications*

#### 1) LABORATORY SCALE FLOW WITH SINUSOIDAL FORCING

As an application of (48) we consider a laboratory scale flow with external parameters as listed in Table 1 for experiment 12. The surface buoyancy flux $B(t)$ is shown graphically in Fig. 18a. With the parameters for experiment 12 we compute, from (50) and (51), an oscillatory response with $K_2 = 0.77B_s$ and $\Phi = -54°$. The response predicted by (48) is shown as a solid line in Fig. 18b and the simulated response from experiment 12 is shown as a dotted line. After a short adjustment interval (not captured by the theory) both amplitude and phase are well aligned. The response at the sill lags the forcing by $t_l = \Phi/\omega = 80$ s.

#### 2) THE SEASONAL RESPONSE IN THE RED SEA

As a second example we consider the response of the Red Sea to seasonal variability in the surface flux $B$. For simplicity we suppose that the evaporation, and associated surface buoyancy flux, varies sinusoidally throughout the year, though more realistic variability could be treated similarly. The Red Sea is known to have a mean annual surface buoyancy flux of somewhere between $B = 2.2 \times 10^{-8}$ m$^2$ s$^{-3}$ (Phillips 1966) and $B = 4.0 \times 10^{-8}$ m$^2$ s$^{-3}$ (Maxworthy 1997) so we will assume an average value of $B_o = 3.1 \times 10^{-8}$ m$^2$ s$^{-3}$ for this example. Since the buoyancy forcing decreases dramatically in summer, we estimate the amplitude of the seasonal oscillation to be $\sim 0.9B_o$. The assumed temporal variation of $B(t)$ over three years is shown in Fig. 19a. Given the dimensions of the Red Sea: $L$ = 2000 km, $W$ = 280 km, $H$ = 150 m (upper circulating layers only), and $h$ = 120 m, the response equation (48) predicts as$_p(t)$ as shown in Fig. 19b. Here we find that the flow at the sill (Strait of Bab al Mandab) reaches a maximum that is only 90% of the corresponding steadily forced value and the response lags the forcing by $t_l$ = 2 months. Assuming the outflow is reasonably described by a two-layer model, and approximating the reduced gravity as $g' = B^{2/3}Lh^{-4/3}$ [see section 2d(3)], the volumetric exchange flow rate $Q = q_sW$ through the Strait of Bab al Mandab is estimated from (29) and is shown graphically in Fig. 19c. Since these predictions are based on scaling laws that have been confirmed only for basins with $L/h \leq 30$, we must emphasize that application to the Red Sea, which has $L/h \sim O(10^4)$, is speculative and approximate. Nevertheless, the mean flow rate of 0.58 Sv (Sv $\equiv 10^6$ m$^3$ s$^{-1}$) and the lag of 2 months are not inconsistent with recent observations in the Strait of Bab al Mandab (Murray and Johns 1997). The assumed amplitude of forcing ($0.9B_o$) produces a seasonal variation in $Q$ of approximately 0.4 Sv, comparable to the estimates of Murray and Johns (1997) and Smeed (1997).

## 6. Conclusions

While steady flow analyses of buoyancy-driven flows are generally informative, they lack what is arguably the most important component of dynamic systems, the time dependence. The analysis methodology developed and applied in sections 4 and 5 can be applied in other circumstances and may prove useful for examining the unsteady dynamics of seasonally forced buoyancy-driven seas, diurnally forced lake side-arms, and other similar systems.

We have shown, using energetics analyses, how a buoyancy-driven basin responds to atmospheric changes. The storage of energy within the basin and flux across open boundaries has been quantified through numerical experimentation. These quantities together determine the transient behavior of the system. By relating the internal variables to known external parameters, the steady-state and time-dependent behavior has been revealed in a generally applicable way.

By simulating the response of $E_p$ and $E_k$ to a step increase in $B$ we determined the relevant timescale of response $t_r$ and the characteristic attenuation coefficient $\alpha = \alpha_*/t_r$. Both of these important quantities may be expressed as functions of the external parameters $B$, $L$, $H$, $W$, and $h$ (see Table 2). This led to a general description of the flow response at the sill for arbitrary unsteady forcing functions (section 5). The response to a sinusoidally varying surface buoyancy flux was predicted for a laboratory scale flow. A comparison between the predicted response and a full numerically simulated flow (Fig. 18) indicated that the amplitude and phase characteristics of the flow are well represented by the theory. Upon closer inspection, we note that the rising and falling arms of the computed response curve differ slightly in slope. This suggests the presence of hysteresis in the system, which might be of interest in future studies. A simple application to the seasonal response in the Red Sea gave reasonable results despite the basin having an aspect ratio $L/h$ orders of magnitude greater than the experimental basins. More detailed comparisons await a set of concurrent forcing and response field measurements, which, to our knowledge, do not yet exist.

*Acknowledgments*

This work was carried out while the first author received funding from an Australian OPRS. Additional support was provided by the U.S. Office of Naval Research (Code 322, Physical Oceanography, N0014-96-1-0616) and the Australian Research Council. We thank Andy Hogg and Ben Hodges for useful comments on an earlier version of the paper.

---

## REFERENCES

Anis A., and J. N. Moum, 1994: Prescriptions for heat flux and entrainment rates in the upper ocean during convection. *J. Phys. Oceanogr*, **24**, 2142–2155. Find this article online

Bray N. A., J. Ochoa, and T. H. Kinder, 1995: The role of the interface in exchange through the Strait of Gibraltar. *J. Geophys. Res*, **100**, 10755–10776. Find this article online

Bryden H. L., and T. H. Kinder, 1991: Steady two-layer exchange through the Strait of Gibraltar. *Deep-Sea Res*, **38**, 445–S463, S. Find this article online

Finnigan T. D., and G. N. Ivey, 1999: Submaximal exchange between a convectively forced basin and a large reservoir. *J. Fluid Mech*, **378**, 357–378. Find this article online

Finnigan T. D., and G. N. Ivey, 2000: Convectively driven exchange flow in a stratified sill-enclosed basin. *J. Fluid Mech*, **418**, 313–338.

Find this article online

Gregg M. C., E. Özsoy, and M. A. Latif, 1999: Quasi-steady exchange flow in the Bosphorus. *Geophys. Res. Lett*, **26**, 83–86. Find this article online

Grimm T., and T. Maxworthy, 1999: Buoyancy-driven meanflow in a long channel with a hydraulically-constrained exit condition. *J. Fluid Mech*, **398**, 155–180. Find this article online

Harashima A., and M. Watanabe, 1986: Laboratory experiments on the steady gravitational circulation excited by cooling of the water surface. *J. Geophys. Res*, **91**, 13056–13064. Find this article online

Kowalik Z., and J. B. Mathews, 1983: Numerical study of the water movement driven by brine rejection from nearshore arctic ice. *J. Geophys. Res*, **88**, 2953–2958. Find this article online

Maxworthy T., 1997: A frictionally and hydraulically constrained model of the convectively driven mean flow in partially enclosed seas. *Deep-Sea Res*, **44**, 1339–1354. Find this article online

Murray S. P., and W. Johns, 1997: Direct observations of seasonal exchange through the Bab al Mandab Strait. *Geophys. Res. Lett*, **24**, 2557–2560. Find this article online

Phillips O. M., 1966: On turbulent convection currents and the circulation of the Red Sea. *Deep-Sea Res*, **13**, 1149–1160. Find this article online

Reid J. L., 1979: On the contribution of Mediterranean Sea outflow to the Norwegian–Greenland Sea. *Deep-Sea Res*, **26**, 1119–1223. Find this article online

Sanford R. S., 1965: *Physical Networks*. Prentice-Hall, 576 pp.

Smeed D., 1997: Seasonal variation of the flow in the strait of Bab al Mandab. *Oceanol. Acta*, **20**, 773–781. Find this article online

Stommel H., and H. G. Farmer, 1953: Control of salinity in an estuary by a transition. *J. Mar. Res*, **12**, 13–20. Find this article online

Sturman J. J., and G. N. Ivey, 1998: Unsteady convective exchange flows in cavities. *J. Fluid Mech*, **368**, 127–153. Find this article online

Winters K. B., and H. Seim, 2000: The role of dissipation and mixing in an exchange flow through a contracting channel. *J. Fluid. Mech*, **407**, 265–290. Find this article online

Winters K. B., H. Seim, and T. D. Finnigan, 2000: Simulation of non-hydrostatic, density-stratified flow in irregular domains. *Int. J. Numer. Methods Fluids*, **32**, 263–284. Find this article online

---

## Tables

TABLE 1. External parameter settings for the numerical experiments (1–12) of the present study and a laboratory experiment (L) of Finnigan and Ivey (2000). The far right column refers to the forcing functions shown in Fig. 3. For experiment 12, $B_s = 0.5 \times 10^{-6}$ m$^2$ s$^{-3}$ and $\omega = 390$ s

| Expt | $L$ (m) | $H$ (m) | $h$ (m) | $W$ (m) | $H/h$ | $B_s$ (m$^2$ s$^{-3}$) | $B_w$ (m$^2$ s$^{-3}$) | Forcing |
|---|---|---|---|---|---|---|---|---|
| 1 | 0.25 | 0.05 | 0.025 | 0.025 | 2.0 | 0 | $1.4 \times 10^{-4}$ | a |
| 2 | 0.25 | 0.05 | 0.025 | 0.025 | 2.0 | $1.4 \times 10^{-4}$ | $1.9 \times 10^{-4}$ | a |
| 3 | 0.25 | 0.05 | 0.025 | 0.025 | 2.0 | $1.9 \times 10^{-4}$ | $1.4 \times 10^{-4}$ | b |
| 4 | 0.25 | 0.05 | 0.025 | 0.025 | 2.0 | $1.9 \times 10^{-4}$ | $2.5 \times 10^{-4}$ | a |
| 5 | 0.46 | 0.05 | 0.025 | 0.025 | 2.0 | 0 | $2.5 \times 10^{-4}$ | a |
| 6 | 0.75 | 0.05 | 0.025 | 0.025 | 2.0 | 0 | $1.6 \times 10^{-4}$ | a |
| 7 | 0.75 | 0.05 | 0.025 | 0.025 | 2.0 | $1.6 \times 10^{-4}$ | $2.1 \times 10^{-4}$ | a |
| 8 | 0.46 | 0.05 | 0.038 | 0.025 | 1.3 | 0 | $2.5 \times 10^{-4}$ | a |
| 9 | 0.25 | 0.10 | 0.075 | 0.025 | 1.3 | 0 | $1.5 \times 10^{-4}$ | a |
| 10 | 0.25 | 0.10 | 0.050 | 0.025 | 2.0 | 0 | $1.5 \times 10^{-4}$ | a |
| 11 | 0.25 | 0.10 | 0.025 | 0.025 | 4.0 | 0 | $1.5 \times 10^{-4}$ | a |
| 12 | 0.25 | 0.05 | 0.025 | 0.025 | 2.0 | $1.4 \times 10^{-4}$ | $B_s \sin(\omega t)$ | c |
| L | 0.25 | 0.04 | 0.025 | — | 1.6 | 0 | $0.4 \times 10^{-4}$ | a |

Click on thumbnail for full-sized image.

TABLE 2. Summary of the main steady-state scaling results. The scaling relations (as numbered in the text) are converted to formulas using the experimentally determined constants

| Scaling | Constants | | Formulas |
|---|---|---|---|
| (22) | $c_q = 2.0 \pm 0.10$ | $\gamma = 1.2 \pm 0.50$ | $E_p = c_q B^{3/2} L^{3/2} H^{1/2} (H/h)^{\gamma}$ |
| (23) | $c_d = 0.2 \pm 0.09$ | $\delta = -0.7 \pm 0.20$ | $E_k = c_d B^{3/2} L^{3/2} H^{1/2} (H/h)^{\delta}$ |
| (28) | $c_t = 0.3 \pm 0.05$ | $\lambda = 1.0 \pm 0.10$ | $\omega_b = c_t B L H^{1/2} (H/h)^{\lambda}$ |
| (32) | $c_f = 0.2 \pm 0.05$ | $\xi = 1.0 \pm 0.10$ | $t_* = c_f L \Delta b^{-1/2} H^{1/2} (H/h)^{\xi}$ |

Click on thumbnail for full-sized image.

TABLE 3. Energy flux and storage quantities for the numerical experiments. Fluxes appear normalized by the forcing flux $sd$, and storage quantities appear normalized by the total stored energy $E_p + E_k$, for each individual experiment

| | | | | | | | | | |
|---|---|---|---|---|---|---|---|---|---|
| 11 | 0.92 | −0.71 | −0.10 | 0.15 | 0.07 | −0.25 | 0.99 | 0.01 |

Click on thumbnail for full-sized image.

## Figures

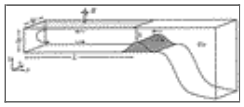

Click on thumbnail for full-sized image.

FIG. 1. A buoyancy-driven marginal sea. A sill at $x = L$ restricts the exchange flow between the sea and the adjoining ocean

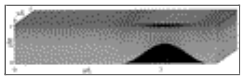

Click on thumbnail for full-sized image.

FIG. 2. Example of a numerical grid used in the simulations. This grid had 129 × 17 × 33 computational nodes. For longer basins, grids with 257 × 17 × 33 nodes were used

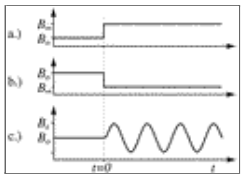

Click on thumbnail for full-sized image.

FIG. 3. The form of the forcing functions used in the present study. The functions shown here are referred to in Table 1

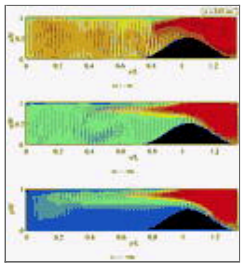

Click on thumbnail for full-sized image.

FIG. 4. Velocity and density fields from experiment 1. (a) At early times the basin interior is occupied by turbulent convection while an exchange flow develops at the sill. (b) As time increases the exchange flow progresses toward the closed end of the basin. (c) Finally, a steady-state is reached when the exchange flow occupies the entire length of the basin. Red indicates lighter fluid and blue indicates heavier fluid. Note how the mean density of the convecting region and thus the outflow over the sill gets progressively more dense with time. For visualization purposes the velocity data have been interpolated onto a coarser grid, relative to the computational grid (see Fig. 2)

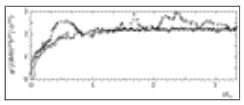

Click on thumbnail for full-sized image.

FIG. 5. Variation with time of the scaled volume flux at the sill crest $q(B/H)^{-1/2}h^{-3/2}$. Results from laboratory experiment L are shown as large circles and results from numerical experiment 1 as small dots. The solid gray curve ($0 \leq t/t_{ss} \leq 0.6$) represents the $t^{1/2}$ scaling of (11), which is consistent with the observed results for both experiments. At about $t/t_{ss} = 1$ the flow reaches a steady state and $q \sim (BL)^{1/3}h$ (solid line)

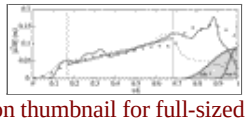

Click on thumbnail for full-sized image.

FIG. 6. Alongchannel variation of the scaled horizontal velocity $|u^3/B|$ in the upper layer. Results from laboratory experiment L are shown as large circles. Results from numerical experiments 1 and 6 are shown as a dotted and solid line, respectively. The shaded objects indicate the width of the sill in each of the numerical experiments. Note how the wider sill affects the velocity variation of experiment 1. Results are consistent with the linear scaling (straight line) in the central region (between the vertical dashed lines)

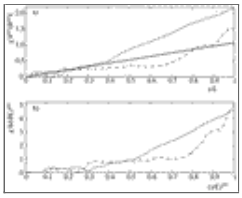

Click on thumbnail for full-sized image.

FIG. 7. Alongchannel variation of $g'$ scaled as suggested by (a) Maxworthy (1997) and (b) Phillips (1966). Results from numerical experiments 1 and 6 are shown as a dashed and dot–dashed line, respectively. The solid line in (a) represents a best fit to the laboratory data presented by Grimm and Maxworthy (1999)

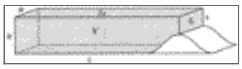

Click on thumbnail for full-sized image.

FIG. 8. Schematic view of the basin control volume

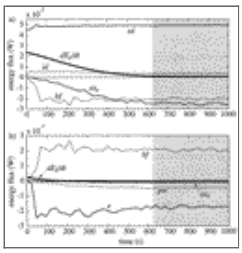

Click on thumbnail for full-sized image.

FIG. 9. Time series for each of the energetics terms. (a) The terms represented in the rate-of-change of potential energy equation (18) and, (b) the terms represented in the rate-of-change of kinetic energy equation (19). Results were derived from experiment 1 for which the flow was initially at rest and of uniform density. The residuals, which indicate how well the energy equations balance, were $O(10^{-10})$ in both (a) and (b)

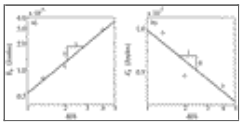

Click on thumbnail for full-sized image.

FIG. 10. Log–log plots of (a) $E_p$ vs $H/h$ and (b) $E_k$ vs $H/h$ for experiments 9–11. The slopes of best-fit lines give estimates of the constants $\gamma$ and $\delta$

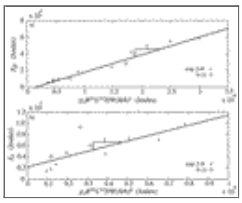

Click on thumbnail for full-sized image.

FIG. 11. (a) Computed values of steady-state stored potential energy $E_p$ in relation to the scaling prediction $\rho_o B^{2/3} L^{5/3} HW(H/h)^{\gamma}$ with the value of $\gamma$ given in Table 2. (b) The analogous relationship between observed $E_k$ and $\rho_o B^{2/3} L^{5/3} HW(H/h)^{\delta}$. Slopes of the fitted lines provide estimates for the proportionality constants, $c_p$ and $c_k$ (see Table 2). Experiment 1 not shown due to redundancy with experiment 3 steady-state results

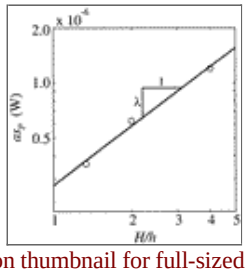


Click on thumbnail for full-sized image.

FIG. 12. Log–log plot of $as_p$ vs $H/h$ for experiments 9–11. The slope of a best-fit line gives an estimate of the constant $\lambda$

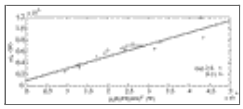

Click on thumbnail for full-sized image.

FIG. 13. Computed values of steady-state advection of potential energy across the sill $as_p$ in relation to the scaling prediction $\rho_o BLHW(H/h)^{\lambda}$ with the value of $\lambda$ given in Table 2. The slope of the fitted line provides an estimate for the proportionality constant $c_s$ (see Table 2). Experiment 1 not shown due to redundancy with experiment 3 steady-state results

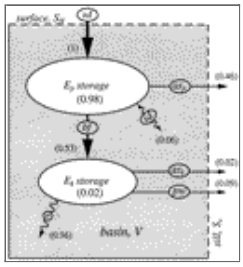

Click on thumbnail for full-sized image.

FIG. 14. Schematic representation of the flux of energy relative to the basin control volume. The bracketed quantities are average steady-state values from experiments 1–7 for $H/h = 2$

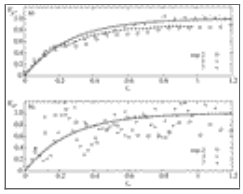

Click on thumbnail for full-sized image.

FIG. 15. Time variation in response to a step increase in $B$ at $t = 0$ of the normalized stored energy quantities (a) $E_{p_*}$ and (b) $E_{k_*}$. The time coordinate is normalized such that $t_* = t/t_r$

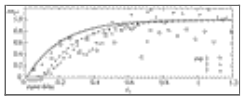

Click on thumbnail for full-sized image.

FIG. 16. Time variation in response to a step increase in $B$ at $t = 0$ of the normalized advection of potential energy across the sill $as_{p_*}$. The time coordinate is normalized such that $t_* = t/t_t$. Note the apparent signal delay indicated by the shifted response curve. This is caused by the finite time required for a change in the surface forcing to be detected at the sill. It is most evident in the results of experiment 7, which had a longer basin

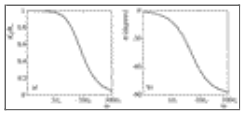

Click on thumbnail for full-sized image.

FIG. 17. Magnitude and phase plots for the response of $as_{p_*}$ as a function of frequency $\omega$. The magnitude has been normalized by its maximum value $B_*$

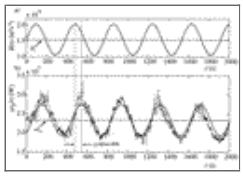

Click on thumbnail for full-sized image.

FIG. 18. Variation of $as_p(t)$ with time in response to a sinusoidal forcing function. (a) Surface buoyancy flux variation. (b) The response of $as_p(t)$. Computed results are shown as small dots and the dimensional form of the response equation (48) is shown

as a solid line

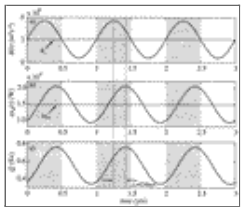

Click on thumbnail for full-sized image.

FIG. 19. Seasonal response of the Red Sea as estimated from likely external forcing parameters and the response equation (48)

*Corresponding author address:* T. D. Finnigan, Department of Oceanography, MSB 434, University of Hawaii at Manoa, 1000 Pope Road, Honolulu, HI 96822.

*Current affiliation: Applied Physics Laboratory, University of Washington, Seattle, Washington.

top